

Improving 3D convolutional neural network comprehensibility via interactive visualization of relevance maps: Evaluation in Alzheimer's disease

Martin Dyrba^{1,*}, Moritz Hanzig^{1,2}, Slawek Altenstein^{3,4}, Sebastian Bader², Tommaso Ballarini⁵, Frederic Brosseron^{5,6}, Katharina Buerger^{7,8}, Daniel Cantré⁹, Peter Dechent¹⁰, Laura Dobisch¹¹, Emrah Düzel^{11,12}, Michael Ewers^{7,8}, Klaus Fliessbach^{5,6}, Wenzel Glanz¹¹, John Dylan Haynes¹³, Michael T. Heneka^{5,6}, Daniel Janowitz⁸, Deniz Baris Keles¹⁴, Ingo Kilimann^{1,15}, Christoph Laske^{16,17,18}, Franziska Maier¹⁹, Coraline D. Metzger^{11,12,20}, Matthias H. Munk^{16,17,18}, Robert Perneczky^{7,21,22,23}, Oliver Peters^{3,14}, Lukas Preis³, Josef Priller^{3,4}, Boris Rauchmann²¹, Nina Roy⁵, Klaus Scheffler²⁴, Anja Schneider^{5,6}, Björn Hendrik Schott^{25,26,27}, Annika Spottke^{5,28}, Eike Jakob Spruth^{3,4}, Marc-André Weber⁹, Birgit Ertl-Wagner^{29,30}, Michael Wagner^{5,6}, Jens Wiltfang^{25,26,31}, Frank Jessen^{5,19,32}, Stefan J. Teipel^{1,15}, for the ADNI[†], AIBL[†], DELCODE[‡] study groups

¹ German Center for Neurodegenerative Diseases (DZNE), Rostock, Germany

² Institute of Visual and Analytic Computing, University of Rostock, Rostock, Germany

³ German Center for Neurodegenerative Diseases (DZNE), Berlin, Germany

⁴ Department of Psychiatry and Psychotherapy, Charité – Universitätsmedizin Berlin, Campus Charité Mitte, Berlin, Germany

⁵ German Center for Neurodegenerative Diseases (DZNE), Bonn, Germany

⁶ Department for Neurodegenerative Diseases and Geriatric Psychiatry, University Hospital Bonn, Bonn, Germany

⁷ German Center for Neurodegenerative Diseases (DZNE), Munich, Germany

⁸ Institute for Stroke and Dementia Research (ISD), University Hospital, Ludwig Maximilian University, Munich, Germany

⁹ Institute of Diagnostic and Interventional Radiology, Pediatric Radiology and Neuroradiology, Rostock University Medical Center, Rostock, Germany

¹⁰ MR-Research in Neurosciences, Georg-August-University, Goettingen, Germany

¹¹ German Center for Neurodegenerative Diseases (DZNE), Magdeburg, Germany

¹² Institute of Cognitive Neurology and Dementia Research (IKND), Otto-von-Guericke University, Magdeburg, Germany

¹³ Bernstein Center for Computational Neuroscience, Berlin, Germany

¹⁴ Department of Psychiatry and Psychotherapy, Charité – Universitätsmedizin Berlin, Campus Benjamin Franklin, Berlin, Germany

¹⁵ Department of Psychosomatic Medicine, Rostock University Medical Center, Rostock, Germany

¹⁶ German Center for Neurodegenerative Diseases (DZNE), Tuebingen, Germany

¹⁷ Section for Dementia Research, Hertie Institute for Clinical Brain Research, Tuebingen, Germany

¹⁸ Department of Psychiatry and Psychotherapy, University of Tuebingen, Tuebingen, Germany

¹⁹ Department of Psychiatry, Medical Faculty, University of Cologne, Cologne, Germany

²⁰ Department of Psychiatry and Psychotherapy, Otto-von-Guericke University, Magdeburg, Germany

²¹ Department of Psychiatry and Psychotherapy, University Hospital, Ludwig Maximilian University, Munich, Germany

²² Munich Cluster for Systems Neurology (SyNergy), Ludwig Maximilian University, Munich, Germany

²³ Ageing Epidemiology Research Unit (AGE), School of Public Health, Imperial College London, London, UK

²⁴ Department for Biomedical Magnetic Resonance, University of Tuebingen, Tuebingen, Germany

²⁵ German Center for Neurodegenerative Diseases (DZNE), Goettingen, Germany

²⁶ Department of Psychiatry and Psychotherapy, University Medical Center Goettingen, Goettingen, Germany

²⁷ Leibniz Institute for Neurobiology, Magdeburg, Germany

²⁸ Department of Neurology, University Hospital Bonn, Bonn

²⁹ Institute for Clinical Radiology, Ludwig Maximilian University, Munich, Germany

³⁰ Department of Medical Imaging, University of Toronto, Toronto, Canada

³¹ Neurosciences and Signaling Group, Institute of Biomedicine (iBiMED), Department of Medical Sciences, University of Aveiro, Aveiro, Portugal

³² Excellence Cluster on Cellular Stress Responses in Aging-Associated Diseases (CECAD), University of Cologne, Cologne, Germany

* Corresponding author. Tel. +49-381-494-9482; Fax: +49-381-9472; mail: martin.dyrba@dzne.de

[†] Data used in preparation of this article were obtained from the Alzheimer's Disease Neuroimaging Initiative (ADNI) database (adni.loni.usc.edu) and the Australian Imaging Biomarkers and Lifestyle Study of Aging (AIBL) database (aibl.csiro.au). As such, the investigators within the ADNI and AIBL contributed to the design and implementation of ADNI and AIBL and/or provided data but did not participate in analysis or writing of this report. A complete listing of ADNI investigators can be found at http://adni.loni.usc.edu/wp-content/uploads/how_to_apply/ADNI_Acknowledgement_List.pdf. AIBL researchers are listed at aibl.csiro.au.

[‡] Data used in this article were provided by the DELCODE study group of the Clinical Research of the German Center for Neurodegenerative Diseases (DZNE). Details can be found at www.dzne.de/en/research/studies/clinical-studies/delcode.

Abstract

Although convolutional neural networks (CNN) achieve high diagnostic accuracy for detecting Alzheimer’s disease (AD) dementia based on magnetic resonance imaging (MRI) scans, they are not yet applied in clinical routine. One important reason for this is a lack of model comprehensibility. Recently developed visualization methods for deriving CNN relevance maps may help to fill this gap as they allow the visualization of key input image features that drive the decision of the model. We investigated whether models with higher accuracy also rely more on discriminative brain regions predefined by prior knowledge. We trained a CNN for the detection of AD in N=663 T1-weighted MRI scans of patients with dementia and amnesic mild cognitive impairment (MCI) and verified the accuracy of the models via cross-validation and in three independent samples including in total N=1655 cases. We evaluated the association of relevance scores and hippocampus volume to validate the clinical utility of this approach. To improve model comprehensibility, we implemented an interactive visualization of 3D CNN relevance maps, thereby allowing intuitive model inspection. Across the three independent datasets, group separation showed high accuracy for AD dementia versus controls ($AUC \geq 0.92$) and moderate accuracy for amnesic MCI versus controls ($AUC \approx 0.75$). Relevance maps indicated that hippocampal atrophy was considered as the most informative factor for AD detection, with additional contributions from atrophy in other cortical and subcortical regions. Relevance scores within the hippocampus were highly correlated with hippocampal volumes (Pearson’s $r \approx -0.81$). The relevance maps highlighted atrophy in regions that we had hypothesized a priori. This strengthens the comprehensibility of the CNN models, which were trained in a purely data-driven manner based on the scans and diagnosis labels. The high hippocampus relevance scores as well as the high performance achieved in independent samples support the validity of the CNN models in the detection of AD-related MRI abnormalities.

Keywords

Alzheimer’s disease, deep learning, convolutional neural network, MRI, layer-wise relevance propagation

Data and code availability statement

Data used for training/evaluation of the models is available from the respective initiatives (ADNI: <http://adni.loni.usc.edu/data-samples/access-data>, AIBL: aibl.csiro.au).

The source code, a demo dataset, the trained CNN models, and all additional files required to run the interactive visualization are publicly available at <https://github.com/martindyrba/DeepLearningInteractiveVis>.

1 Introduction

Alzheimer’s disease (AD) is characterized by widespread neuronal degeneration, which manifests macroscopically as cortical atrophy that can be detected *in vivo* using structural magnetic resonance imaging (MRI) scans. Particularly at earlier stages of AD, atrophy patterns are relatively regionally specific, with volume loss in the medial temporal lobe (MTL) and particularly the hippocampus being the best-established MRI marker for diagnosing Alzheimer’s disease at the dementia stage as well as at its prodromal stage amnesic mild cognitive impairment (MCI) [1, 2]. Automated detection of subtle

brain changes in early stages of Alzheimer’s disease could improve diagnostic confidence and early access to intervention [1, 3].

Convolutional neural networks (CNN) provide a powerful method for image recognition. Various studies have evaluated the performance of CNN for the detection of Alzheimer’s disease in MR images with promising results regarding both separation of diagnostic groups and the prediction of conversion from MCI to manifest dementia (Table 1). Despite the high accuracy levels achieved by CNN models, a major drawback is their algorithmic complexity, which renders them black-box systems. The poor intuitive comprehensibility of CNNs is one of the major obstacles hindering the application in clinical settings. In the context of explainable artificial intelligence, different terms evolved with respect to the degree of human understanding about the decision-making process: *interpretable models* are assumed to be computationally simple or easily understandable, such as logistic regression or decision trees; *comprehensible models* are expected to provide informative symbols or visualizations the user can reason over, such as relevance maps; and *explainable models* genuinely provide explanations of the decision making process in a human-understandable way, for example by automatically generating flow charts or textual descriptions [4, 5].

Novel methods for deriving relevance maps from CNN models [6, 7] may help to overcome the black-box problem. In general, relevance or saliency maps indicate the amount of information or contribution of a single input feature on the probability of a particular output class. Previous methodological approaches like gradient-weighted class activation mapping (Grad-CAM) [8], occlusion sensitivity analyses [9, 10], and local interpretable model-agnostic explanations (LIME) [11] had the limitation that deriving the relevance or saliency maps provided only group-average estimates, required long runtime [12] or provided only low spatial resolution [13, 14]. In contrast, more recent methods such as guided backpropagation [15] or layer-wise relevance propagation (LRP) [6, 7] use back-tracing of neural activation through the network paths to obtain high-resolution relevance maps. An overview of neuroimaging studies which applied these methods in the context of AD is provided in Table 1 (see last column).

Recently, three studies compared LRP with other CNN visualization methods for the detection of Alzheimer’s disease in T1-weighted MRI scans [13, 14, 16]. The derived relevance maps showed strongest contribution of medial and lateral temporal lobe atrophy, which matched the *a priori* expected brain regions of high diagnostic relevance [17, 18]. Böhle and colleagues [16] pioneered the application of LRP in neuroimaging and reported a high sensitivity of this method to actual regional atrophy. That means, LRP showed a much stronger dependency of regional relevance scores on the diagnostic group than the guided backpropagation algorithm used for comparison. Their findings are in line with [19], which reported that guided backpropagation and some other methods are insufficient with respect to provide information associated with the actual class or diagnosis rather than general input image properties. Unfortunately, [19] did not include LRP in their analysis. Eitel and colleagues [14] assessed the stability and reproducibility of CNN performance results and LRP relevance maps. After training ten individual models based on the same training dataset, they reported the highest consistency and lowest deviation of relevance maps for LRP and guided backpropagation among five different methods [14]. Recently, we compared various methods for relevance and saliency attribution [13]. Visually, all tested methods provided similar relevance maps except for Grad-CAM, which provided much lower spatial resolution, and, hence, lost a high amount of regional specificity. For the other methods, the main difference was the amount “negative” relevance which indicates evidence against a particular diagnostic class.

Notably, [14] and [16] did not include patients in the prodromal stage of MCI and [13] focused on a limited range of coronal slices covering the temporal lobe. All three studies did not validate their results

in independent samples. Therefore, it remained an open question, if the CNN models provide a sufficient accuracy level across samples and at the same time yield reasonable relevance maps for individual people such that this approach could be used as basis for neuroradiological assistance systems.

In the current study, our aims were threefold: First, we trained robust CNN models that achieved a high diagnostic accuracy in three independent validation samples. Second, we designed and implemented a visualization software to interactively derive and inspect diagnostic relevance maps from CNN models for individual patients. Here, we expected high relevance to be shown in brain regions with strong disease-related atrophy, primarily in the medial temporal lobe. Third, we evaluated the validity of relevance maps in terms of correlation of hippocampus relevance scores and hippocampus volume, which is the best-established MRI marker for Alzheimer's disease [17, 18]. We expected a high consistency of both measures, which would strengthen the overall comprehensibility of the CNN models.

Table 1 Overview of previous studies applying neural networks for the detection of AD and MCI

Study (chronologic order)	Data type	Sample	Algorithm	Performance	Addressed model comprehensibility
Suk et al. (2014) [20]	MRI GM & FDG-PET	93 AD, 76 MCIC, 128 MCInc, and 101 CN	RBM on class discriminative patches learnt by statistical significance tests	Accuracy: CN/AD 95.35% CN/MCI 85.67% MCIC/MCInc 74.58%	Yes ¹
Li et al. (2015) [21]	MRI & FDG-PET	51 AD, 43 MCIC, 56 MCInc, and 52 CN	RBM for feature learning and SVM for classification	Accuracy: CN/AD 91.4% CN/MCI 77.4%	No
Ortiz et al. (2016) [22]	MRI GM & FDG-PET	70 AD, 64 MCInc, MCIC 39, and 68 CN	RBM for feature learning and SVM for classification	Accuracy and AUC: CN/AD 90% and 0.95 CN/MCIC 83% and 0.95	Yes ²
Aderghal et al. (2018) [23]	MRI & DTI	188 AD, 399 MCI, and 228 CN	CNN for hippocampus region of interest only	Accuracy: CN/AD 92.5% CN/MCI 82.9%	No
Liu et al. (2018a) [24]	FDG-PET	93 AD, 146 MCI and 100 CN	CNN and RNN	Accuracy and AUC: CN/AD 91.2% and 0.95 CN/MCI 78.9% and 0.84	Yes ³
Liu et al. (2018b) [25]	MRI	199 AD and 229 CN	CNN on landmarks selected by statistical significance tests	Accuracy And AUC: CN/AD 90.56% and 0.96	Partly ⁴
Lin et al. (2018) [26]	MRI	188 AD, 229 CN, 169 MCIC, and 193 MCInc	CNN	Accuracy and AUC: CN/AD 88.79% MCIC/MCInc 79.9% and 0.86	No
Böhle et al. (2019) [16]	MRI	211 AD and 169 CN	CNN	Accuracy: CN/AD 87.96%	Yes ⁵
Li et al. (2019) [27]	MRI	Training: 192 AD, 383 MCI and 228 CN Test: 225 AD, 479 MCI and 639 CN	CNN for hippocampus only	AUC: CN/AD 0.96 MCIC/MCInc 0.75 for one year conversion and 0.81 for three years conversion	Yes ⁶
Dyrba et al. (2020) [13]	MRI	189 AD, 219 MCI and 254 CN	CNN for coronal hippocampus slices only	AUC: CN/AD 0.93, CN/MCI 0.75	Yes ⁷
Lian et al. (2020) [28]	MRI	Training: 199 AD and 229 CN Test: 159 AD and 200 CN	CNN	Accuracy and AUC: CN/AD 90.3% and 0.95	Yes ⁸
Qiu et al. (2020) [29]	MRI	Training: 188 AD and 229 CN	FCN	AUC: CN/AD 0.92, 0.87, 0.89, 0.88	Yes ³

		Test: 3 samples including 300 AD and 749 CN		Accuracy: CN/AD 83%, 87%, 77%, 82%	
Wen et al. (2020) [30]	MRI	Training: 336 AD, 295 MCIC, 298 MCInc, 330 AD Test: 76 AD, 20 MCIC, 13 MCInc, 429 CN	CNN	Accuracy: CN/AD 86% MCIC/MCInc 74%	No
Thibeau-Sutre et al. (2020) [10]	MRI	Training: 336 AD and 330 CN Test: 76 AD and 429 CN	CNN	Accuracy: CN/AD 90%	Yes ³
Jo et al. [31]	Tau-PET	66 AD and, 66 CN	CNN	Accuracy: CN/AD 90.8%	Yes ⁵

¹) Visualization of selected features (image patches) and RBM model weights projected on MRI scan.

²) Visualization of SVM model weights projected on MRI scan.

³) Visualization of most contributing brain areas obtained from occlusion sensitivity analysis.

⁴) Visualization of top 50 anatomical landmarks used as input for the CNN.

⁵) Visualization of LRP relevance maps and comparison of relevance scores by group and brain region.

⁶) Visualization of most contributing hippocampus areas obtained from CNN class activation mapping.

⁷) Visualization of LRP and other methods' relevance maps and comparison by diagnostic group.

⁸) Visualization of most contributing image areas obtained from CNN class activation mapping.

AD: Alzheimer's dementia, MCI: mild cognitive impairment, MCIC: MCI converted to dementia, MCInc: non-converter/stable MCI, CN: cognitively normal controls, DTI: diffusion tensor imaging, FCN: fully connected network, RBM: restricted Boltzmann machine, RNN: recurrent neural network, CNN: convolutional neural network, MRI: T1-weighted magnetic resonance imaging, GM: gray matter volume, FDG-PET: glucose metabolism derived from fluorodeoxyglucose positron emission tomography.

2 Materials and Methods

2.1 Study samples

Data for **training** the CNN models were obtained from the Alzheimer's Disease Neuroimaging Initiative (ADNI) database (<https://adni.loni.usc.edu>). The ADNI was launched in 2003 by the National Institute on Aging, the National Institute of Biomedical Imaging and Bioengineering, the Food and Drug Administration, private pharmaceutical companies, and non-profit organizations, with the primary goal of testing whether neuroimaging, neuropsychological, and other biological measurements can be used as reliable in vivo markers of Alzheimer's disease pathogenesis. A complete description of ADNI, up-to-date information, and a summary of diagnostic criteria are available at <https://www.adni-info.org>. We selected a sample of N=663 participants from the ADNI-GO and ADNI-2 phases, based on the availability of concurrent T1-weighted MRI and amyloid AV45-PET scans. Notably, we used only one (i.e., the first) available scan from each ADNI participant in our analyses. The sample characteristics are shown in Table 2. We included 254 cognitively normal controls, 220 patients with (late) amnesic mild cognitive impairment (MCI), and 189 patients with Alzheimer's dementia (AD). Amyloid-beta status of the participants was determined by the UC Berkeley [32] based on the AV45-PET standardized uptake value ratio (SUVR) cutoff 1.11.

For **validation** of the diagnostic accuracy of the CNN models, we obtained MRI scans from three independent cohorts. The sample characteristics and demographic information are summarized in Table 2. The first dataset was compiled from N=575 participants of the recent ADNI-3 phase. The second dataset included MR images from N=606 participants of the Australian Imaging, Biomarker & Lifestyle Flagship Study of Ageing (AIBL) (<https://aibl.csiro.au>), provided via the ADNI system. A summary of the diagnostic criteria and additional information is available at

<https://aibl.csiro.au/about>. For AIBL, we additionally obtained amyloid PET scans which were available for 564 participants (93%). The PET scans were processed using the Centiloid SPM pipeline and converted to Centiloid values as recommended for the different amyloid PET tracers [33-35]. Amyloid-beta status of the participants was determined using the cutoff 24.1 CL [34]. As a third sample, we included data from N=474 participants of the German Center for Neurodegenerative Diseases (DZNE) multicenter observational study on Longitudinal Cognitive Impairment and Dementia (DELCODE) [36]. Comprehensive information on the diagnostic criteria and study design are provided in [36]. For the DELCODE sample, cerebrospinal fluid (CSF) biomarkers were available for a subsample of 227 participants (48%). Amyloid-beta status was determined using the A β 42/A β 40 ratio with a cutoff 0.09 [36].

Table 2 Summary of sample characteristics.

Sample	CN	MCI	AD
ADNI-GO/2 (Training) N=663			
Sample size (female)	254 (130)	220 (93)	189 (80)
Age (SD)	75.4 (6.6)	74.1 (8.1)	75.0 (8.0)
Education (SD)	16.4 (2.7)	16.2 (2.8)	15.9 (2.7)
MMSE (SD)	29.1 (1.2)	27.6 (1.9)	22.6 (3.2)
RAVLT Delayed recall (SD)	7.6 (4.1)	3.2 (3.7)	0.8 (1.9)
WMS-LM Delayed recall (SD)	13.9 (3.7)	5.1 (3.8)	1.5 (2.1)
Hippocampus volume (SD) mm ³	6,235 (756)	5,619 (963)	4,834 (930)
Amyloid status (neg/pos)	177/77	79/141	28/161
ADNI-3 (Validation) N=575			
Sample size (female)	326 (211)	187 (85)	62 (27)
Age (SD)	70.0 (7.5)	72.2 (7.5)	74.8 (7.7)
Education (SD)	16.6 (2.2)	16.6 (2.5)	16.5 (2.4)
MMSE (SD)	29.1 (1.1)	27.8 (2.0)	23.1 (3.3)
RAVLT Delayed recall (SD)	8.3 (4.4)	4.7 (4.7)	0.3 (0.9)
WMS-LM Delayed recall (SD)	13.0 (3.5)	7.2 (3.9)	2.0 (2.8)
Hippocampus volume (SD) mm ³	6,583 (649)	6,112 (902)	4,839 (978)
AIBL (Validation) N=606			
Sample size (female)	448 (260)	96 (46)	62 (36)
Age (SD)	72.4 (6.2)	74.3 (6.9)	73.2 (7.3)
MMSE (SD)	28.7 (1.2)	27.0 (2.2)	21.2 (5.3)
WMS-LM Delayed recall (SD)	11.2 (4.3)	4.9 (4.0)	1.0 (1.9)
Hippocampus volume (SD) mm ³	6,362 (704)	5,712 (1,028)	4,940 (1,055)
Amyloid status (neg/pos)	316/101	34/54	6/53
DELCODE (Validation) N=474			
Sample size (female)	215 (124)	155 (72)	104 (61)
Age (SD)	69.5 (5.5)	73.0 (5.7)	75.2 (6.2)
Education (SD)	14.7 (2.7)	14.0 (3.1)	12.9 (3.1)
MMSE (SD)	29.5 (0.8)	27.8 (2.0)	23.1 (3.2)
WMS-LM Delayed recall (SD)	14.3 (3.6)	7.4 (5.2)	1.8 (2.8)
Hippocampus volume (SD) mm ³	6,543 (679)	5,665 (950)	4,610 (944)
Amyloid status (neg/pos)	58/28	30/57	5/49

Years of education were not available for the AIBL dataset. RAVLT delayed recall scores were not available for the AIBL and DELCODE samples.

2.2 Image preparation and processing

All MRI scans were preprocessed using the Computational Anatomy Toolbox (CAT12, v9.6/r7487) [37] for Statistical Parametric Mapping 12 (SPM12, v12.6/r1450, Wellcome Centre for Human Neuroimaging, London, UK). Images were segmented into grey and white matter, spatially normalized to the default CAT12 brain template in Montreal Neurological Institute (MNI) reference space using the DARTEL algorithm, resliced to an isotropic voxel size of 1.5 mm, and modulated to adjust for expansion and shrinkage of the tissue. Initially and after all processing steps, all scans were visually inspected to check for image quality. All scans were cleaned for the effects of the covariates age, sex, total intracranial volume (TIV) and scanner magnetic field strength (FS) using linear regression. This step was performed, as these factors are known to effect the voxel intensities or regional brain volume [38, 39]. For each voxel vx_{ij} , linear models were fitted on the healthy controls of the respective samples: $vx_{ij} = \beta_{i0} + \beta_{i1}age_j + \beta_{i2}sex_j + \beta_{i3}TIV_j + \beta_{i4}FS_j + \epsilon_{ij}$, with i being the voxel index, j being the participant index, β_i being the respective model coefficients (for each voxel), and ϵ_i being the error term or residual. Subsequently, the predicted voxel intensities were subtracted from all participants' gray matter maps to obtain the residual images: $res_{ij} = vx_{ij} - (\beta_{i0} + \beta_{i1}age_j + \beta_{i2}sex_j + \beta_{i3}TIV_j + \beta_{i4}FS_j)$. This method was applied as brain volume, specifically in temporal lobe and hippocampus, is substantially decreasing/shrinking in old age independently of the disease process [38, 39] and we expected this approach to increase accuracy. As sensitivity analysis, we also repeated CNN training on the raw gray matter volume maps for comparison. Patients with MCI and AD were combined into one disease-positive group. On the one hand, this was done as we observed a low sensitivity of machine learning models for MCI when trained only on AD cases, due to the much larger and more heterogeneous patterns of atrophy in AD than in MCI, where atrophy is specifically present in medial temporal and parietal regions [40]. On the other hand, combining both groups substantially increased the training sample, which was required to reduce overfitting of the CNN models.

2.3 CNN model structure and training

The CNN layer structure was adapted from [16] and [30], which was inspired by the prominent 2D image detection networks AlexNet [41] and VGG [42]. The model was implemented in Python 3.7 with Keras 2.2.4 and Tensorflow 1.15. The layout is shown in Figure 1. The residualized 3D images with a resolution of 100x100x120 voxels were fed as input into the neural network and processed by three consecutive convolution blocks including 3D convolutions (5 filters of 3x3x3 kernel size) with rectified linear activation function (ReLU), maximum pooling (2x2x2 voxel patches), and batch normalization layers (Figure 1). Then, three fully connected layers with ReLU activation and dropout (10%) followed, each consisting of 64, 32, and 2 neurons, respectively. The weights of last two layers were regularized with the L2 norm penalty and the last layer had the softmax activation function that rescaled the class activation values to likelihood scores. The network required approximately 700,000 parameters to be estimated.

The whole CNN pipeline was evaluated by stratified twentyfold cross-validation, partitioning the ADNI-GO/2 sample into approximately 630 training and 35 test images with almost equal distribution of CN, MCI, and AD cases. Additionally, data augmentation was used to increase the training sets. All images included in the respective training subsamples were flipped along the coronal (L/R) axis and also translated by ± 10 voxels in each direction (x/y/z), yielding fourteen times increased training sets of approximately 8,800 images. The CNN model was then trained with the ADAM optimizer, applying the categorical cross-entropy loss function and the default learning rate of 0.001. To speed up training, we defined an early stopping of the training if the model accuracy on the training data did not improve for at least two training epochs. Thus, training finished after nine or ten epochs for all folds. On a Windows 10 computer with Intel Core i5-9600 hexa-core CPU, 64 GB working memory, and NVIDIA GeForce GTX 1650 CUDA GPU, training took approximately 35 minutes per fold and 12 hours in total. All twenty

models were saved to disk for further inspection and validation. As control analysis, we also repeated the whole procedure based on the raw image data (normalized gray matter volumes) instead of using the residuals as CNN input.

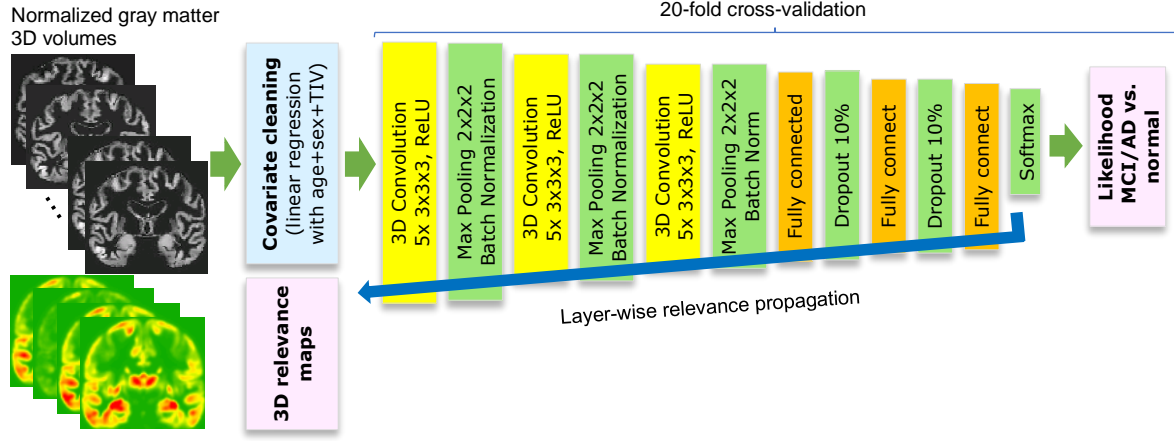


Figure 1 Data flow chart and convolutional neural network structure.

2.4 Model evaluation

The mean accuracy and area under the receiver operating characteristic curve (AUC) were calculated on the respective cross-validation test subsamples, which were completely excluded from the CNN training process. Additionally, an ‘optimized accuracy’ was derived from the CNN likelihood scores for the test images and test sample AUC analysis. This was based on the Youden index, which determined the optimal threshold for test set likelihood scores that maximized the difference between the true positive rate and false positive rate. Although this optimized accuracy generally tends to overestimate the actual group discrimination ability of a model, it provides the upper bound of the accuracy that can be achieved by that particular model.

Several studies reported excellent diagnostic accuracy for CNN to detect AD and MCI based on neuroimaging data (Table 1). However, [30] reviewed numerous papers and identified a potential bias of the reported model performances in almost half of the papers (17 out of 33) due to insufficient validation or data leakage in the worst case, i.e. when test set scans were included in parameter optimization procedures. To avoid such issues, we performed evaluation of the model performance on three independent datasets in addition to the classical cross-validation procedure. Notably, the covariate cleaning was run for each sample independently, but regression parameters were estimated only on the subsample of cognitively normal control participants.

As internal validity benchmark, we compared CNN model performance and group separation using hippocampus volume, the best-established MRI marker for Alzheimer’s disease. Automated extraction of hippocampus volume is already implemented in commercial radiology software to aid physicians in diagnosing dementia. We extracted total hippocampus volume from the modulated and normalized MRI scans using the Harvard-Oxford subcortical atlas [43]. The extracted volumes were corrected for the effects of age, sex, total intracranial volume, and magnetic field strength of the MRI scanner in the same way as described above for the CNN input. Here, a linear model was estimated based on the normal controls, and then the parameters were applied to the measures of all participants to obtain the residuals. Subsequently, the residuals were entered into a receiver operating characteristic analysis to obtain the AUC and the optimal threshold with highest accuracy based on the Youden index.

Additionally, we report AUC confidence intervals derived from the package pROC (1.16.2) for R (3.6.0), which were estimated based on 2,000 bootstrap replicates.

2.5 CNN relevance map visualization

Relevance maps were derived from the CNN models using the LRP algorithm [6] implemented in the Python package iNNvestigate 1.0.8 [44]. LRP has previously been demonstrated to yield relevance maps with high spatial resolution and clinical plausibility [13, 16]. In this approach, the final network activation scores for a given input image are propagated back through the network layers. LRP applies a relevance conservation principle, that means that the total amount of relevance per layer are kept constant during the back tracing procedure to reduce numerical challenges that occur in other methods [6]. Several rules exist, which apply different weighting to positive (excitatory) and negative (inhibitory) connections such that network activation for and against a specific class can be considered differentially. Here, we applied the so-called $\alpha=1, \beta=0$ rule that only considers positive relevance as proposed by [13, 16]. In this case, the relevance of a network neuron R_j was calculated from all connected neurons k in the subsequent network layer using the formula $R_j = \sum_k [a_j w_{jk}^+ R_k / \sum_j (a_j w_{jk}^+)]$, with a_j being the activation of neuron j , w_{jk}^+ being the positive weight of the connection between neurons j and k , and R_k being the relevance attributed to neuron k [7].

To facilitate model assessment and quick inspection of relevance maps, we implemented an interactive Python visualization application that is capable of immediate switching between CNN models and participants. More specifically, we used the Bokeh Visualization Library 1.4.0 (<https://bokeh.org>). Bokeh provides a webserver backend and web browser frontend to directly run Python code that dynamically generates interactive websites containing various graphical user interface components and plots. The Bokeh web browser JavaScript libraries handle the communication between the browser and server instance and translate website user interaction into Python function calls. In this way we implemented various visualization components to adjust plotting parameters and provide easy navigation for the 2D slice views obtained from the 3D MRI volume.

The application is structured following a model-view-controller paradigm. An overview of implemented functions is provided in Supplementary Figure 2. A sequence diagram illustrating function calls when selecting a new person is provided in Supplementary Figure 3. The source code and files required to run the interactive visualization are publicly available via <https://github.com/martindyrba/DeepLearningInteractiveVis>.

As core functionality we implemented the visualization in a classical 2D multi-slice window with axial, coronal and sagittal views, cross-hair, and sliders to adjust the relevance threshold as well as minimum cluster size threshold (see Figure 2 below). Additionally, we added visual guides to improve usability, including (a) a histogram providing the distribution of cluster sizes next to the cluster size threshold slider, (b) plots visualizing the amount of positive and negative relevance per slice next to the slice selection sliders, and (c) statistical information on the currently selected cluster. Further, assuming spatially normalized MRI data in MNI reference space, we added (d) atlas-based anatomical region lookup for the current cursor/cross-hair position and (e) the option to display the outline of the anatomical region to simplify visual comparison with the cluster location.

2.6 CNN model comprehensibility and validation

As quantitative metrics for assessing relevance map quality are still missing, we compared CNN relevance scores in the hippocampus with hippocampus volume. Here, we used the same hippocampus masks as mentioned above for deriving hippocampus volume, and applied it on the relevance maps obtained from all ADNI-GO/2 participants for each model. The sum of relevance score

of each voxel inside the mask was considered as hippocampus relevance. Hippocampus relevance and volume were compared using Pearson's correlation coefficient.

Additionally, we visually examined a large number of scans from each group to derive common relevance patterns and match them with the original MRI scans. Further, we calculated mean relevance maps for each group.

3 Results

3.1 Group separation

The accuracy and AUC for diagnostic group separation are shown in Table 3 and additional performance measures provided in Supplementary Table 1. The CNN reached an optimized accuracy between 85.9 % and 90.9 % across samples with an AUC between 0.919 and 0.958 for separating AD and controls. For MCI vs. controls, the group separation was substantially lower with optimized accuracies between 67.4 % and 76.0 % and an AUC between 0.667 and 0.842. Notably, these values were almost identical compared to the group separation performance of hippocampus volume (Table 3). The performance results for the raw gray matter volume data as input for the CNN are provided in Supplementary Table 2. In direct comparison to the CNN results for the residualized data, the AUC was lower for the raw data with a difference of 2.6 % on average, but with a variation between samples: a difference of 3.9 % for ADNI2, 4.9 % for ADNI3, 2.2 % for AIBL, and 0.4 % for DELCODE (Table 3, Supplementary Table 2).

Table 3 Group separation performance for hippocampus volume and the convolutional neural network models.

Sample	Hippocampus volume (residuals*)		3D convolutional neural network		
	Accuracy	AUC (CI)	Accuracy (SD)	Opt. accuracy (SD)	AUC (SD)
ADNI-GO/2					
MCI vs. CN	72.6 %	0.767 (0.725–0.809)	69.0 % (9.7)	73.2 % (8.1)	0.770 (0.103)
AD vs. CN	88.0 %	0.943 (0.920–0.962)	77.5 % (4.9)	88.3 % (6.0)	0.944 (0.058)
MCI ⁺ vs. CN ⁻	79.6 %	0.837 (0.790–0.880)	75.0 % (12.2)	76.0 % (8.8)	0.842 (0.114)
AD ⁺ vs. CN ⁻	89.9 %	0.952 (0.929–0.972)	80.9 % (6.8)	85.9 % (8.9)	0.958 (0.054)
ADNI-3					
MCI vs. CN	67.6 %	0.683 (0.633–0.733)	63.7 % (2.9)	67.4 % (3.2)	0.667 (0.016)
AD vs. CN	90.7 %	0.939 (0.898–0.972)	72.5 % (6.2)	88.5 % (3.2)	0.919 (0.015)
AIBL					
MCI vs. CN	76.1 %	0.740 (0.676–0.799)	69.7 % (5.2)	78.6 % (4.5)	0.731 (0.019)
AD vs. CN	83.9 %	0.918 (0.864–0.961)	73.7 % (6.3)	87.7 % (4.2)	0.926 (0.009)
MCI ⁺ vs. CN ⁻	81.1 %	0.740 (0.680–0.800)	73.0 % (5.5)	85.1 % (3.4)	0.813 (0.028)
AD ⁺ vs. CN ⁻	86.4 %	0.918 (0.868–0.961)	76.2 % (6.0)	90.5 % (2.8)	0.958 (0.009)
DELCODE					
MCI vs. CN	74.3 %	0.769 (0.718–0.817)	66.8 % (2.5)	70.9 % (1.9)	0.731 (0.022)
AD vs. CN	92.5 %	0.940 (0.903–0.972)	75.9 % (4.7)	89.2 % (1.5)	0.928 (0.011)
MCI ⁺ vs. CN ⁻	80.9 %	0.872 (0.801–0.936)	70.6 % (3.4)	74.1 % (2.5)	0.796 (0.023)
AD ⁺ vs. CN ⁻	93.5 %	0.954 (0.899–0.995)	79.2 % (4.8)	90.9 % (1.7)	0.947 (0.012)

* Group separation based on hippocampus volume corrected for effects of the covariates age, sex, total intracranial volume and MRI scanner field strength using a linear model.

3.2 Model comprehensibility and relevance map visualization

The implemented web application frontend is displayed in Figure 2. In the left column, the user can select a study participant and a specific model. Below, there are controls (sliders) to adjust the thresholds for displayed relevance score, cluster size, and overlay transparency. As we used the spatially normalized MRI images as CNN input, we can directly obtain the anatomical reference location label from the automated anatomical labeling (AAL) atlas [45] given the MNI coordinates at the specific crosshair location, which is displayed in the light blue box. The green box displays statistics on the currently selected relevance cluster such as number of voxels and respective volume. In the middle part of Figure 2, the information used as covariates (age, sex, total intracranial volume) and the CNN likelihood score for AD are depicted above the coronal, axial, and sagittal views of the 3D volume. We further added sliders and plots of cumulated relevance score per slices as visual guides to facilitate navigation to slices with high relevance. All user interactions are directly sent to the server, evaluated internally, and updated in the respective views and control components in real-time without major delay. For instance, adjusting the relevance threshold directly changes the displayed brain views, the shape of the red relevance summary plots, and blue cluster size histogram. A sequence diagram of internal function calls when selecting a new participant is illustrated in Supplementary Figure 3.

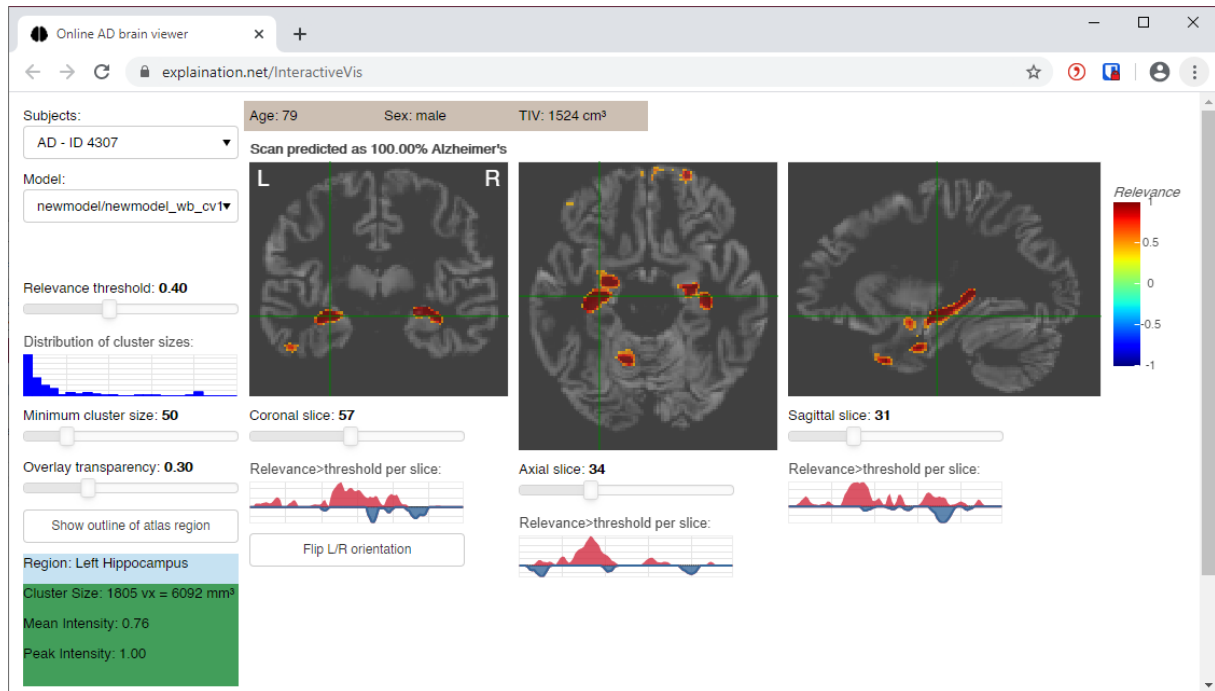


Figure 2 Web application to interactively examine the neural network relevance maps for individual MRI scans.

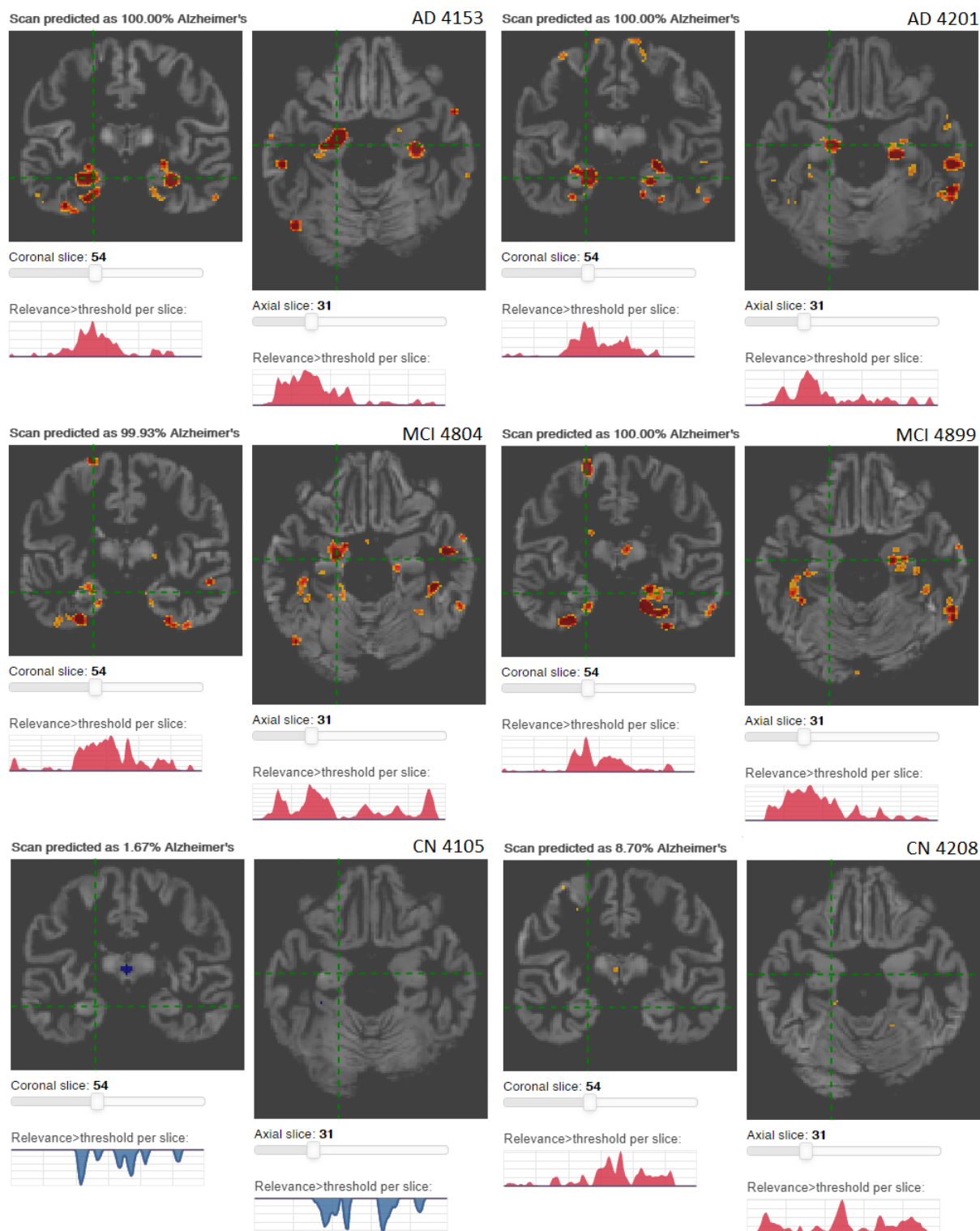


Figure 3 Example relevance maps obtained for different people. Top row: Alzheimer's dementia patients, middle row: patients with mild cognitive impairment, bottom row: cognitively normal controls.

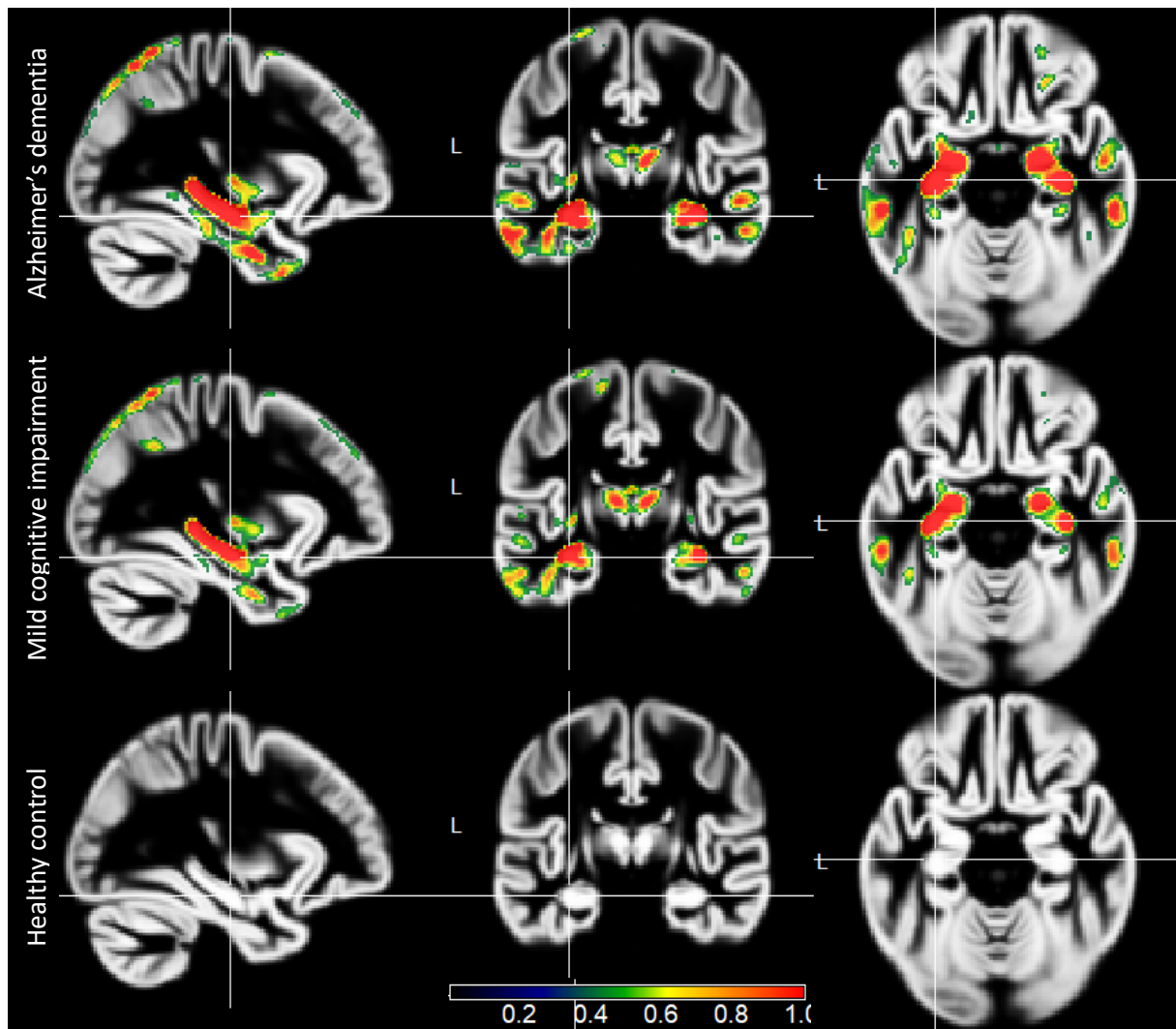


Figure 4 Mean relevance maps for Alzheimer's dementia patients (top row), patients with mild cognitive impairment (middle row), and healthy controls (bottom row). Relevance maps thresholded at 0.4 for better comparison.

Individual people's relevance maps are illustrated in Figure 3. The group mean relevance maps are shown in Figure 4 and in Supplementary Figure 1. They are very similar to traditional statistical maps obtained from voxel-based morphometry, indicating the highest contribution of medial temporal brain regions, more specifically hippocampus, amygdala, thalamus, and middle temporal gyrus.

The correlation of individual patient's hippocampus relevance score and hippocampus volume for one of the twenty cross-validation models is displayed in Figure 5. For this model, the correlation was $r = -0.85$ for bilateral hippocampus volume. When considering only the left hemisphere (i.e., correlation of left hippocampus relevance and left volume), the correlation was identical ($r_L = -0.85$). For the right hemisphere, the correlation was slightly lower ($r_R = -0.82$). Across all twenty models, the median correlation of total hippocampus relevance and volume was $r = -0.81$ with a range of -0.85 and $+0.44$. Notably, one CNN model with $r = 0.44$ failed to detect MCI ($AUC = 0.50$), although achieving a high AUC for dementia ($AUC = 0.90$). Inspection of the relevance maps revealed a strong focus of this particular model on widespread frontal and parietal, but almost no temporal regions, suggesting that this model ignored hippocampus atrophy for deriving its decision. To test whether hippocampus volume and relevance measures were biased due to using the same mask, we assessed their correlation in healthy

controls only. Here, the dependency was substantially lower with $r_{CN} = -0.11$. To test the consistency of hippocampus relevance scores across all twenty CNN models obtained from the cross-validation strategy, we assessed the median correlation coefficient of hippocampus relevance for all pairwise model comparisons. It was $r = 0.88$, indicating a high agreement between models.

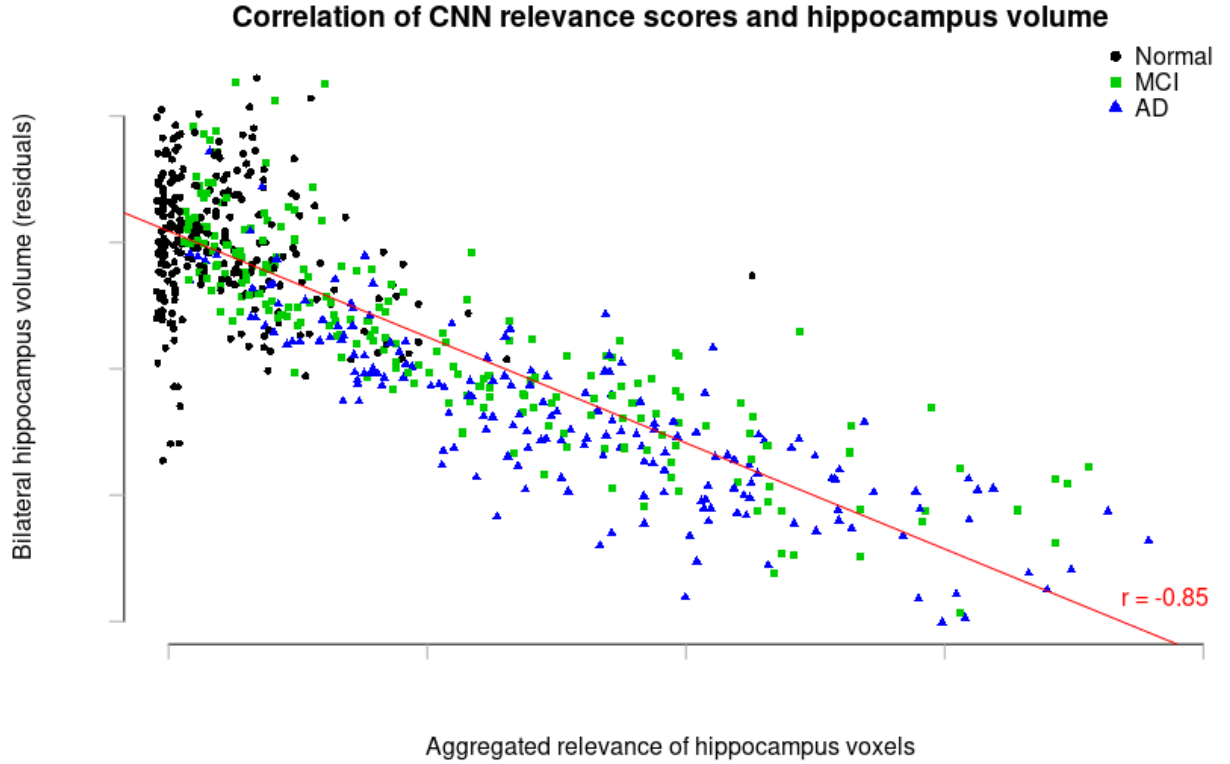


Figure 5 Scatter plot and correlation of bilateral hippocampus volume and neural network relevance scores for the hippocampus regions ($r = -0.85$, $p < 0.001$).

4 Discussion

4.1 Neural network comprehensibility

We have presented a CNN framework and interactive visualization application for obtaining class-specific relevance maps for disease detection in MRI scans, yielding human-interpretable and clinically plausible visualizations of key features for image discrimination. To date, most CNN studies focus on parameter estimation and model development (see e.g. [30] for a review and a comparison of CNN accuracies reached for different types of input data). Model development and optimization are undoubtedly important tasks, and there are still several challenges to tackle. However, as black-box models, it is typically not feasible to judge, why a CNN fails or which image features drive a particular decision of the network. This gap might be closed with the use of novel visualization algorithms such as LRP [6] and deep Taylor decomposition [7]. In our application, CNN relevance maps provided a useful tool for model inspection to reveal the brain regions which contributed most to the decision process encoded by the neural network models.

Currently, there is no ground truth information for relevance maps, and there are no appropriate methods available to quantify relevance map quality. Samek and colleagues [46] proposed the information-theoretic measures relevance map entropy and complexity, which mainly characterize the scatter or smoothness of images. Further, adapted from classical neural network sensitivity analysis,

they assessed the robustness of relevance maps using perturbation testing where small image patches were replaced by random noise, which was also applied in [19]. However, already for 2D data, this method is computationally very expensive and only practical for a limited number of input images. Based on the extensive knowledge about the effect of Alzheimer’s disease on brain volume as presented in T1-weighted MRI scans [17, 18], we selected a direct quantitative comparison of relevance maps with hippocampus volume as validation method. Here, we obtained very high correlations between hippocampus relevance scores and volume (median correlation $r = -0.81$), underlining the clinical plausibility of learnt patterns to differentiate AD and MCI patients from controls. In addition, visual inspection of relevance maps also revealed several other clusters with gray matter atrophy in the individual patients’ images that contributed to the decision of the CNN (Figure 2). Böhle and colleagues [16] proposed an atlas-based aggregation of CNN relevance maps to be used as ‘disease fingerprints’ and to enable a quick comparison between patients and controls, a concept that has also been proposed previously for differential diagnosis of dementia based on heterogeneous clinical data and other machine learning models [47, 48].

Notably, the CNN models presented here were solely based on the combinations of input images with their corresponding diagnostic labels to determine which brain features were diagnostically relevant. Traditionally, extensive clinical experience is required to define relevant features (e.g., hippocampus volume) that discriminate between a clinical population (here: AD, MCI) and a healthy control group. Also, typically only few predetermined parameters are used (e.g., hippocampus volume or medial temporal lobe atrophy score [17, 18]). Our results demonstrate that the combination of CNN and relevance map approaches constitutes a promising tool for improving the utility of CNN in the classification of MRIs of patients with suspected AD in a clinical context. By referring back to the relevance maps, trained clinicians will be enabled to compare classification results to comprehensible features visible in the relevance images and thereby more readily interpret the classification results in clinically ambiguous situations. Perspectively, the relevance map approach might also provide a helpful tool to reveal features for more complex diagnostic challenges such as differential diagnosis between various types of dementia, for instance the differentiation between AD, frontotemporal dementia, and dementia with Lewy bodies.

4.2 CNN performance

As expected, CNN-based classification reached an excellent $AUC \geq 0.9$ for the group separation of AD compared to controls but a substantially lower accuracy for group separation between MCI and controls ($AUC \approx 0.75$, Table 3). When restricting the classification to amyloid-positive MCI versus amyloid-negative controls, group separation improved to $AUC = 0.84$ in ADNI-GO/2 and 0.80 in DELCODE, highlighting the heterogeneity of MCI as diagnostic entity and the importance of biomarker stratification [1, 2]. In summary, these numbers are also reflected by the recent CNN literature as shown in Table 1. Notably, [30] reported several limitations and issues in the performance evaluation of some other CNN papers, such that it is not easy to finally conclude on the group separation capabilities of the CNN models in realistic settings. To overcome such challenges, we validated the models on three large independent cohorts (Table 3), providing strong evidence for their generalizability and for the robustness of our CNN approach.

To put the CNN model performance into perspective, we compared the accuracy of the CNN models with the accuracy achieved by assessing hippocampus volume, the key clinical MRI marker for neurodegeneration in Alzheimer’s disease [1, 2]. Interestingly, there were only minor differences in the achieved AUC values across all samples (Table 3). The MCI group of the ADNI-3 sample, which yielded the worst group separation of all samples ($AUC = 0.67$), was actually the group with the largest average hippocampus volumes and, therefore, the lowest group difference compared to the controls (Table 2). Obviously, our results here indicate a limited value of using CNN models instead of traditional

volumetric markers for the detection of Alzheimer's dementia and mild cognitive impairment. Previous MRI CNN paper have not reported the baseline accuracy reached by hippocampus volume for comparison. However, as noted above, CNN might provide a useful tool to derive discriminative features for complex diagnostic tasks, for instance for the differential diagnosis between various types of dementia.

As already mentioned above, CNN performance estimation and model robustness are still open challenges. Wen and colleagues [30] actually showed only a minor effect of the particular CNN model parameterization, network layer configuration, or type of input data on the final accuracy, which means that the fully trained CNN models achieve almost identical performance. However, it is not yet assessed how model complexity and the number of layers influence the model comprehensibility and relevance map visualization. As most important factor for CNN training, [30] identified the amount of available training data to obtain a robust and reliable CNN. Here, different CNN approaches exist for MRI data [30] based on i) 2D convolutions for single slices, often reusing pre-trained models for general image detection, such as AlexNet [41] and VGG [42]; ii) so-called 2.5D approaches running 2D convolutions on each of the three slice orientations, which are then combined at higher layers of the network; and iii) 3D convolutions, which are at least theoretically superior in detecting texture and shape features in any direction of the 3D volume. Although final accuracy is almost comparable between all three approaches for detecting MCI and AD [30], the 3D models require substantially more parameters to be estimated during training. For instance, a single 2D convolutional kernel has $3 \times 3 = 9$ parameters whereas the 3D version requires $3 \times 3 \times 3 = 27$ parameters. Here, relevance maps will enable the assessment of learnt CNN models with respect to overfitting to clinically irrelevant brain regions and the detection of potential biases present in the training samples, which cannot be directly identified just from the model accuracy.

4.3 Future prospects

Several studies focused on CNN models for the integration of multimodal imaging data, e.g. MRI and fluorodeoxyglucose (FDG)-PET [20-22], or heterogeneous clinical data [49]. In this context, relevance mapping visualization approaches need to be developed that allow for direct comparison of the relevance magnitude for images and clinical variables simultaneously. Another aspect is the automated generation of textual descriptions and diagnostic explanations from images [50-52]. Given the recent technical progress, we suggest that the approach is now ready for interdisciplinary exchange to assess how clinicians can benefit from CNN assistance in their diagnostic workup, and which requirements must be met to increase clinical utility. Beyond the technical challenges, regulatory and ethical aspects and caveats must be carefully considered when introducing CNN as part of clinical decision support systems and medical software – and the discussion of these issues has just recently begun [53, 54].

4.4 Conclusion

We presented a framework for obtaining diagnostic relevance maps from CNN models to improve model comprehensibility. These relevance maps have revealed reproducible and clinically plausible atrophy patterns in AD and MCI patients, with high correlation with the well-established MRI marker of hippocampus volume. The implemented web application allows a quick and versatile inspection of brain regions with a high relevance score in individuals. With the increased comprehensibility of CNNs provided by the relevance maps, the data-driven and hypothesis-free CNN modeling approach might provide a useful tool to aid differential diagnosis of dementia and other neurodegenerative diseases, where fine-grained knowledge on discriminating brain alterations is still missing.

References

1. Jack CR, Albert MS, Knopman DS, McKhann GM, Sperling RA, Carrillo MC, Thies B, Phelps CH: Introduction to the recommendations from the National Institute on Aging-Alzheimer's Association workgroups on diagnostic guidelines for Alzheimer's disease. *Alzheimer's & Dementia* 2011, 7(3):257-262.
2. Dubois B, Feldman HH, Jacova C, Hampel H, Molinuevo JL, Blennow K, DeKosky ST, Gauthier S, Selkoe D, Bateman R *et al*: Advancing research diagnostic criteria for Alzheimer's disease: the IWG-2 criteria. *The Lancet Neurology* 2014, 13(6):614-629.
3. Vemuri P, Fields J, Peter J, Klöppel S: Cognitive interventions in Alzheimer's and Parkinson's diseases. *Current Opinion in Neurology* 2016, 29(4):405-411.
4. Lipton ZC: The Mythos of Model Interpretability. *Queue* 2018, 16(3):31-57.
5. Doran D, Schulz S, Besold TR: What Does Explainable AI Really Mean?: A New Conceptualization of Perspectives. In: *CEUR Workshop Proceedings*. vol. 2071; 2017: 1–8.
6. Bach S, Binder A, Montavon G, Klauschen F, Müller K-R, Samek W: On Pixel-Wise Explanations for Non-Linear Classifier Decisions by Layer-Wise Relevance Propagation. *Plos One* 2015, 10(7).
7. Montavon G, Samek W, Müller K-R: Methods for interpreting and understanding deep neural networks. *Digital Signal Processing* 2018, 73:1-15.
8. Selvaraju RR, Cogswell M, Das A, Vedantam R, Parikh D, Batra D: Grad-CAM: Visual Explanations from Deep Networks via Gradient-Based Localization. In: *2017 IEEE International Conference on Computer Vision (ICCV)*. 2017: 618-626.
9. Zeiler MD, Fergus R: Visualizing and Understanding Convolutional Networks. In: *Computer Vision – ECCV 2014*. 2014: 818-833.
10. Thibeau-Sutre E, Colliot O, Dormont D, Burgos N, Landman BA, Išgum I: Visualization approach to assess the robustness of neural networks for medical image classification. In: *Medical Imaging 2020: Image Processing*. 2020.
11. Ribeiro MT, Singh S, Guestrin C: "Why Should I Trust You?". In: *Proceedings of the 22nd ACM SIGKDD International Conference on Knowledge Discovery and Data Mining*. 2016: 1135-1144.
12. Alber M: Software and Application Patterns for Explanation Methods. In: *Explainable AI: Interpreting, Explaining and Visualizing Deep Learning*. 2019: 399-433.
13. Dyrba M, Pallath AH, Marzban EN: Comparison of CNN Visualization Methods to Aid Model Interpretability for Detecting Alzheimer's Disease. In: *Bildverarbeitung für die Medizin*. 2020: 307-312.
14. Eitel F, Ritter K: Testing the Robustness of Attribution Methods for Convolutional Neural Networks in MRI-Based Alzheimer's Disease Classification. In: *Interpretability of Machine Intelligence in Medical Image Computing and Multimodal Learning for Clinical Decision Support*. 2019: 3-11.
15. Springenberg JT, Dosovitskiy A, Brox T, Riedmiller M: Striving for Simplicity: The All Convolutional Net. In: *3rd International Conference on Learning Representations, ICLR 2015, Workshop Track Proceedings*. Edited by Bengio Y, LeCun Y.
16. Böhle M, Eitel F, Weygandt M, Ritter K: Layer-Wise Relevance Propagation for Explaining Deep Neural Network Decisions in MRI-Based Alzheimer's Disease Classification. *Frontiers in aging neuroscience* 2019, 11:194.
17. Scheltens P, Leys D, Barkhof F, Huglo D, Weinstein HC, Vermersch P, Kuiper M, Steinling M, Wolters EC, Valk J: Atrophy of medial temporal lobes on MRI in "probable" Alzheimer's disease and normal ageing: diagnostic value and neuropsychological correlates. *Journal of Neurology, Neurosurgery & Psychiatry* 1992, 55(10):967-972.
18. Teipel S, Drzezga A, Grothe MJ, Barthel H, Chételat G, Schuff N, Skudlarski P, Cavedo E, Frisoni GB, Hoffmann W *et al*: Multimodal imaging in Alzheimer's disease: validity and usefulness for early detection. *The Lancet Neurology* 2015, 14(10):1037-1053.
19. Adebayo J, Gilmer J, Muelly M, Goodfellow I, Hardt M, Kim B: Sanity Checks for Saliency Maps. In: *Proceedings of the 32nd International Conference on Neural Information Processing Systems (NIPS'18)*. Red Hook, NY, USA: Curran Associates Inc; 2018: 9525–9536.
20. Suk H-I, Lee S-W, Shen D: Hierarchical feature representation and multimodal fusion with deep learning for AD/MCI diagnosis. *NeuroImage* 2014, 101:569-582.
21. Li F, Tran L, Thung K-H, Ji S, Shen D, Li J: A Robust Deep Model for Improved Classification of AD/MCI Patients. *IEEE Journal of Biomedical and Health Informatics* 2015, 19(5):1610-1616.
22. Ortiz A, Munilla J, Gorris JM, Ramirez J: Ensembles of Deep Learning Architectures for the Early Diagnosis of the Alzheimer's Disease. *International journal of neural systems* 2016, 26(7):1650025.

23. Aderghal K, Khvostikov A, Krylov A, Benois-Pineau J, Afdel K, Catheline G: Classification of Alzheimer Disease on Imaging Modalities with Deep CNNs Using Cross-Modal Transfer Learning. In: *2018 IEEE 31st International Symposium on Computer-Based Medical Systems (CBMS)*. 2018: 345-350.
24. Liu M, Cheng D, Yan W: Classification of Alzheimer's Disease by Combination of Convolutional and Recurrent Neural Networks Using FDG-PET Images. *Frontiers in Neuroinformatics* 2018, 12.
25. Liu M, Zhang J, Nie D, Yap P-T, Shen D: Anatomical Landmark Based Deep Feature Representation for MR Images in Brain Disease Diagnosis. *IEEE Journal of Biomedical and Health Informatics* 2018, 22(5):1476-1485.
26. Lin W, Tong T, Gao Q, Guo D, Du X, Yang Y, Guo G, Xiao M, Du M, Qu X: Convolutional Neural Networks-Based MRI Image Analysis for the Alzheimer's Disease Prediction From Mild Cognitive Impairment. *Frontiers in Neuroscience* 2018, 12.
27. Li H, Habes M, Wolk DA, Fan Y: A deep learning model for early prediction of Alzheimer's disease dementia based on hippocampal magnetic resonance imaging data. *Alzheimer's & Dementia* 2019, 15(8):1059-1070.
28. Lian C, Liu M, Zhang J, Shen D: Hierarchical Fully Convolutional Network for Joint Atrophy Localization and Alzheimer's Disease Diagnosis Using Structural MRI. *IEEE Transactions on Pattern Analysis and Machine Intelligence* 2020, 42(4):880-893.
29. Qiu S, Joshi PS, Miller MI, Xue C, Zhou X, Karjadi C, Chang GH, Joshi AS, Dwyer B, Zhu S *et al*: Development and validation of an interpretable deep learning framework for Alzheimer's disease classification. *Brain* 2020, 143(6):1920-1933.
30. Wen J, Thibeau-Sutre E, Diaz-Melo M, Samper-González J, Routier A, Bottani S, Dormont D, Durrleman S, Burgos N, Colliot O: Convolutional neural networks for classification of Alzheimer's disease: Overview and reproducible evaluation. *Medical Image Analysis* 2020, 63.
31. Jo T, Nho K, Risacher SL, Saykin AJ: Deep learning detection of informative features in tau PET for Alzheimer's disease classification. *BMC Bioinformatics* 2020, 21(S21).
32. Landau SM, Mintun MA, Joshi AD, Koeppe RA, Petersen RC, Aisen PS, Weiner MW, Jagust WJ: Amyloid deposition, hypometabolism, and longitudinal cognitive decline. *Annals of Neurology* 2012, 72(4):578-586.
33. Klunk WE, Koeppe RA, Price JC, Benzinger TL, Devous MD, Jagust WJ, Johnson KA, Mathis CA, Minhas D, Pontecorvo MJ *et al*: The Centiloid Project: Standardizing quantitative amyloid plaque estimation by PET. *Alzheimer's & Dementia* 2015, 11(1):1-15.e14.
34. Navitsky M, Joshi AD, Kennedy I, Klunk WE, Rowe CC, Wong DF, Pontecorvo MJ, Mintun MA, Devous MD: Standardization of amyloid quantitation with florbetapir standardized uptake value ratios to the Centiloid scale. *Alzheimer's & Dementia* 2018, 14(12):1565-1571.
35. Battle MR, Pillay LC, Lowe VJ, Knopman D, Kemp B, Rowe CC, Doré V, Villemagne VL, Buckley CJ: Centiloid scaling for quantification of brain amyloid with [18F]flutemetamol using multiple processing methods. *EINMMI Research* 2018, 8(1).
36. Jessen F, Spottke A, Boecker H, Brosseron F, Buerger K, Catak C, Fließbach K, Franke C, Fuentes M, Heneka MT *et al*: Design and first baseline data of the DZNE multicenter observational study on predementia Alzheimer's disease (DELCODE). *Alzheimer's Research & Therapy* 2018, 10(1).
37. Kurth F, Gaser C, Luders E: A 12-step user guide for analyzing voxel-wise gray matter asymmetries in statistical parametric mapping (SPM). *Nature Protocols* 2015, 10(2):293-304.
38. Dima D, Modabbernia A, Papachristou E, Doucet GE, Agartz I, Aghajani M, Akudjedu TN, Albajes-Eizagirre A, Alnæs D, Alpert KI *et al*: Subcortical volumes across the lifespan: Data from 18,605 healthy individuals aged 3–90years. *Human Brain Mapping* 2021.
39. Jack CR, Wiste HJ, Weigand SD, Knopman DS, Vemuri P, Mielke MM, Lowe V, Senjem ML, Gunter JL, Machulda MM *et al*: Age, Sex, and APOE ϵ 4 Effects on Memory, Brain Structure, and β -Amyloid Across the Adult Life Span. *JAMA Neurology* 2015, 72(5).
40. Grothe MJ, Teipel SJ: Spatial patterns of atrophy, hypometabolism, and amyloid deposition in Alzheimer's disease correspond to dissociable functional brain networks. *Human Brain Mapping* 2016, 37(1):35-53.
41. Krizhevsky A, Sutskever I, Hinton GE: ImageNet Classification with Deep Convolutional Neural Networks. In: *Advances in Neural Information Processing Systems* 25. Edited by Pereira F, Burges CJC, Bottou L, Weinberger KQ: Curran Associates, Inc; 2012: 1097–1105.
42. Simonyan K, Zisserman A: Very Deep Convolutional Networks for Large-Scale Image Recognition. In: *3rd International Conference on Learning Representations (ICLR 2015)*. Edited by Bengio Y, LeCun Y; 2015.
43. Desikan RS, Ségonne F, Fischl B, Quinn BT, Dickerson BC, Blacker D, Buckner RL, Dale AM, Maguire RP, Hyman BT *et al*: An automated labeling system for subdividing the human cerebral cortex on MRI scans into gyral based regions of interest. *NeuroImage* 2006, 31(3):968-980.
44. Alber M, Lapuschkin S, Seegerer P, Hägele M, Schütt KT, Montavon G, Samek W, Müller K-R, Dähne S, Kindermans P-J: iNNvestigate Neural Networks! *Journal of Machine Learning Research* 2019, 20:1–8.

45. Tzourio-Mazoyer N, Landeau B, Papathanassiou D, Crivello F, Etard O, Delcroix N, Mazoyer B, Joliot M: Automated Anatomical Labeling of Activations in SPM Using a Macroscopic Anatomical Parcellation of the MNI MRI Single-Subject Brain. *NeuroImage* 2002, 15(1):273-289.
46. Samek W, Binder A, Montavon G, Lapuschkin S, Muller K-R: Evaluating the Visualization of What a Deep Neural Network Has Learned. *IEEE Transactions on Neural Networks and Learning Systems* 2017, 28(11):2660-2673.
47. Tolonen A, Rhodius-Meester HFM, Bruun M, Koikkalainen J, Barkhof F, Lemstra AW, Koene T, Scheltens P, Teunissen CE, Tong T *et al*: Data-Driven Differential Diagnosis of Dementia Using Multiclass Disease State Index Classifier. *Frontiers in Aging Neuroscience* 2018, 10.
48. Bruun M, Frederiksen KS, Rhodius-Meester HFM, Baroni M, Gjerum L, Koikkalainen J, Urhema T, Tolonen A, van Gils M, Rueckert D *et al*: Impact of a clinical decision support tool on prediction of progression in early-stage dementia: a prospective validation study. *Alzheimer's Research & Therapy* 2019, 11(1).
49. Candemir S, Nguyen XV, Prevedello LM, Bigelow MT, White RD, Erdal BS, Neuroimaging Initiative AsD: Predicting rate of cognitive decline at baseline using a deep neural network with multidata analysis. *Journal of Medical Imaging* 2020, 7(04).
50. Jing B, Xie P, Xing E: On the Automatic Generation of Medical Imaging Reports. In: *Proceedings of the 56th Annual Meeting of the Association for Computational Linguistics (Volume 1: Long Papers)*. 2018: 2577-2586.
51. Zhang Z, Xie Y, Xing F, McGough M, Yang L: MDNet: A Semantically and Visually Interpretable Medical Image Diagnosis Network. In: *IEEE Conference on Computer Vision and Pattern Recognition (CVPR)* 2017: 6428–6436.
52. Lucieri A, Bajwa MN, Braun SA, Malik MI, Dengel A, Ahmed S: On Interpretability of Deep Learning based SkinLesion Classifiers using Concept Activation Vectors. In: *International Joint Conference on Neural Networks International Joint Conference on Neural Networks (IJCNN-2020), July 19-24, Glasgow, United Kingdom*. IEEE; 2020.
53. Proposed Regulatory Framework for Modifications to Artificial Intelligence/Machine Learning (AI/ML)-Based Software as a Medical Device (SaMD) [<https://www.fda.gov/media/122535/download>]
54. Ethics Guidelines for Trustworthy AI [https://ec.europa.eu/newsroom/dae/document.cfm?doc_id=60419]

Acknowledgements

The data samples were provided by the DELCODE study group of the Clinical Research Unit of the German Center for Neurodegenerative Diseases (DZNE). Details and participating sites can be found at www.dzne.de/en/research/studies/clinical-studies/delcode. The DELCODE study was supported by Max Delbrück Center for Molecular Medicine in the Helmholtz Association (MDC), Berlin; Center for Cognitive Neuroscience Berlin (CCNB) at Freie Universität Berlin; Bernstein Center for Computational Neuroscience (BCCN), Berlin; Core Facility MR-Research in Neurosciences, University Medical Center Goettingen; Institute for Clinical Radiology, Ludwig Maximilian University, Munich; Institute of Diagnostic and Interventional Radiology, Pediatric Radiology and Neuroradiology, Rostock University Medical Center; and Magnetic Resonance research center, University Hospital Tuebingen.

Data collection and sharing for this project was funded by the Alzheimer's Disease Neuroimaging Initiative (ADNI) (National Institutes of Health Grant U01 AG024904). ADNI is funded by the National Institute on Aging, the National Institute of Biomedical Imaging and Bioengineering, and through generous contributions from the following: AbbVie, Alzheimer's Association; Alzheimer's Drug Discovery Foundation; Araclon Biotech; BioClinica, Inc.; Biogen; Bristol-Myers Squibb Company; CereSpir, Inc.; Cogstate; Eisai Inc.; Elan Pharmaceuticals, Inc.; Eli Lilly and Company; EuroImmun; F. Hoffmann-La Roche Ltd and its affiliated company Genentech, Inc.; Fujirebio; GE Healthcare; IXICO Ltd.; Janssen Alzheimer Immunotherapy Research & Development, LLC.; Johnson & Johnson Pharmaceutical Research & Development LLC.; Lumosity; Lundbeck; Merck & Co., Inc.; Meso Scale Diagnostics, LLC.; NeuroRx Research; Neurotrack Technologies; Novartis Pharmaceuticals Corporation; Pfizer Inc.; Piramal Imaging; Servier; Takeda Pharmaceutical Company; and Transition Therapeutics. The Canadian Institutes of Health Research is providing funds to support ADNI clinical sites in Canada. Private sector contributions are facilitated by the Foundation for the National Institutes of Health (www.fnih.org). The grantee organization is the Northern California Institute for Research and Education, and the study is coordinated by the Alzheimer's Therapeutic Research Institute at the University of Southern California. ADNI data are disseminated by the Laboratory for Neuro Imaging at the University of Southern California.

Ethics approval

Data collecting within ADNI and AIBL were approved by participating institutions. See <https://adni.loni.usc.edu> and <https://aibl.csiro.au> for details. The DELCODE study was approved by participating institutions. See [36] for details. The retrospective analysis, study design and interactive visualization of relevance maps was approved by the internal review board of the Rostock University Medical Center, reference number A 2020-0182.

Competing interests

The authors declare no conflict of interest.

Authors' contributions

MD: conceptualization, methodology, data curation and processing, coding and software development, visualization, writing of the original draft. MH: coding and software development, visualization. ST: conceptualization, methodology, data collection and curation, writing, review and editing, supervision and clinical validation. All others: data acquisition, collection and curation, substantial intellectual contribution on study design and methodology, review and editing, clinical validation. All authors read and approved the final manuscript.

Supplementary material

Supplementary Table 1 Group separation performance for hippocampus volume and the convolutional neural network models (extended) for residualized data.

Sample	Hippocampus volume (residuals*)		3D convolutional neural network												
	Accuracy	AUC (CI)	Accuracy (SD)	Sensitivity (SD)	Specificity (SD)	F1-score (SD)	Positive predictive value (SD)	Negative predictive value (SD)	Opt. accuracy (SD)	Opt. sensitivity (SD)	Opt. specificity (SD)	Opt. F1-score (SD)	Opt. positive predictive value (SD)	Opt. negative predictive value (SD)	AUC (SD)
ADNI-GO/2															
MCI vs. CN	72.6 %	0.767 (0.725–0.809)	69.0 % (9.7)	0.732 (0.181)	0.658 (0.124)	0.671 (0.112)	0.652 (0.121)	0.757 (0.117)	73.2 % (8.1)	0.645 (0.128)	0.814 (0.178)	0.695 (0.089)	0.797 (0.156)	0.729 (0.058)	0.770 (0.103)
AD vs. CN	88.0 %	0.943 (0.920–0.962)	77.5 % (4.9)	0.926 (0.095)	0.658 (0.124)	0.759 (0.074)	0.679 (0.088)	0.935 (0.083)	88.3 % (6.0)	0.876 (0.119)	0.814 (0.178)	0.826 (0.108)	0.810 (0.152)	0.906 (0.087)	0.944 (0.058)
MCI ⁺ vs. CN ⁺	79.6 %	0.837 (0.790–0.880)	75.0 % (12.2)	0.831 (0.172)	0.654 (0.194)	0.709 (0.154)	0.671 (0.169)	0.847 (0.146)	76.0 % (8.8)	0.638 (0.214)	0.896 (0.137)	0.706 (0.199)	0.852 (0.173)	0.761 (0.126)	0.842 (0.114)
AD ⁺ vs. CN ⁺	89.9 %	0.952 (0.929–0.972)	80.9 % (6.8)	0.947 (0.088)	0.654 (0.194)	0.754 (0.136)	0.731 (0.126)	0.931 (0.131)	85.9 % (8.9)	0.818 (0.251)	0.896 (0.137)	0.813 (0.215)	0.886 (0.140)	0.857 (0.177)	0.958 (0.054)
ADNI-3															
MCI vs. CN	67.6 %	0.683 (0.633–0.733)	63.7 % (2.9)	0.542 (0.065)	0.691 (0.079)	0.600 (0.021)	0.509 (0.046)	0.725 (0.010)	67.4 % (3.2)	0.484 (0.117)	0.783 (0.112)	0.579 (0.055)	0.586 (0.078)	0.729 (0.021)	0.667 (0.016)
AD vs. CN	90.7 %	0.939 (0.898–0.972)	72.5 % (6.2)	0.907 (0.047)	0.691 (0.079)	0.780 (0.041)	0.368 (0.063)	0.976 (0.010)	88.5 % (3.2)	0.864 (0.060)	0.783 (0.112)	0.813 (0.048)	0.466 (0.120)	0.969 (0.010)	0.919 (0.015)
AIBL															
MCI vs. CN	76.1 %	0.740 (0.676–0.799)	69.7 % (5.2)	0.616 (0.072)	0.714 (0.074)	0.654 (0.029)	0.324 (0.046)	0.897 (0.011)	78.6 % (4.5)	0.528 (0.090)	0.841 (0.072)	0.639 (0.050)	0.441 (0.088)	0.894 (0.011)	0.731 (0.019)

AD vs. CN	83.9 %	0.918 (0.864–0.961)	73.7 % (6.3)	0.904 (0.032)	0.714 (0.074)	0.795 (0.039)	0.315 (0.061)	0.982 (0.005)	87.7 % (4.2)	0.854 (0.062)	0.841 (0.072)	0.843 (0.022)	0.454 (0.108)	0.977 (0.008)	0.926 (0.009)
MCI ⁺ vs. CN ⁻	81.1 %	0.740 (0.680–0.800)	73.0 % (5.5)	0.731 (0.070)	0.730 (0.073)	0.724 (0.029)	0.325 (0.051)	0.941 (0.011)	85.1 % (3.4)	0.630 (0.071)	0.888 (0.048)	0.733 (0.040)	0.516 (0.109)	0.934 (0.009)	0.813 (0.028)
AD ⁺ vs. CN ⁻	86.4 %	0.918 (0.868–0.961)	76.2 % (6.0)	0.951 (0.025)	0.730 (0.073)	0.823 (0.041)	0.382 (0.067)	0.989 (0.005)	90.5 % (2.8)	0.888 (0.059)	0.888 (0.048)	0.885 (0.020)	0.592 (0.107)	0.980 (0.009)	0.958 (0.009)
DELCODE															
MCI vs. CN	74.3 %	0.769 (0.718–0.817)	66.8 % (2.5)	0.645 (0.079)	0.684 (0.079)	0.656 (0.028)	0.601 (0.041)	0.730 (0.027)	70.9 % (1.9)	0.553 (0.081)	0.821 (0.064)	0.654 (0.041)	0.699 (0.054)	0.720 (0.025)	0.731 (0.022)
AD vs. CN	92.5 %	0.940 (0.903–0.972)	75.9 % (4.7)	0.914 (0.026)	0.684 (0.079)	0.779 (0.044)	0.590 (0.059)	0.944 (0.012)	89.2 % (1.5)	0.874 (0.027)	0.821 (0.064)	0.845 (0.027)	0.711 (0.071)	0.931 (0.011)	0.928 (0.011)
MCI ⁺ vs. CN ⁻	80.9 %	0.872 (0.801–0.936)	70.6 % (3.4)	0.741 (0.079)	0.671 (0.093)	0.695 (0.041)	0.694 (0.048)	0.729 (0.044)	74.1 % (2.5)	0.631 (0.105)	0.850 (0.088)	0.713 (0.048)	0.822 (0.082)	0.706 (0.043)	0.796 (0.023)
AD ⁺ vs. CN ⁻	93.5 %	0.954 (0.899–0.995)	79.2 % (4.8)	0.936 (0.019)	0.671 (0.093)	0.777 (0.062)	0.711 (0.058)	0.925 (0.018)	90.9 % (1.7)	0.905 (0.040)	0.850 (0.088)	0.873 (0.035)	0.846 (0.081)	0.916 (0.026)	0.947 (0.012)

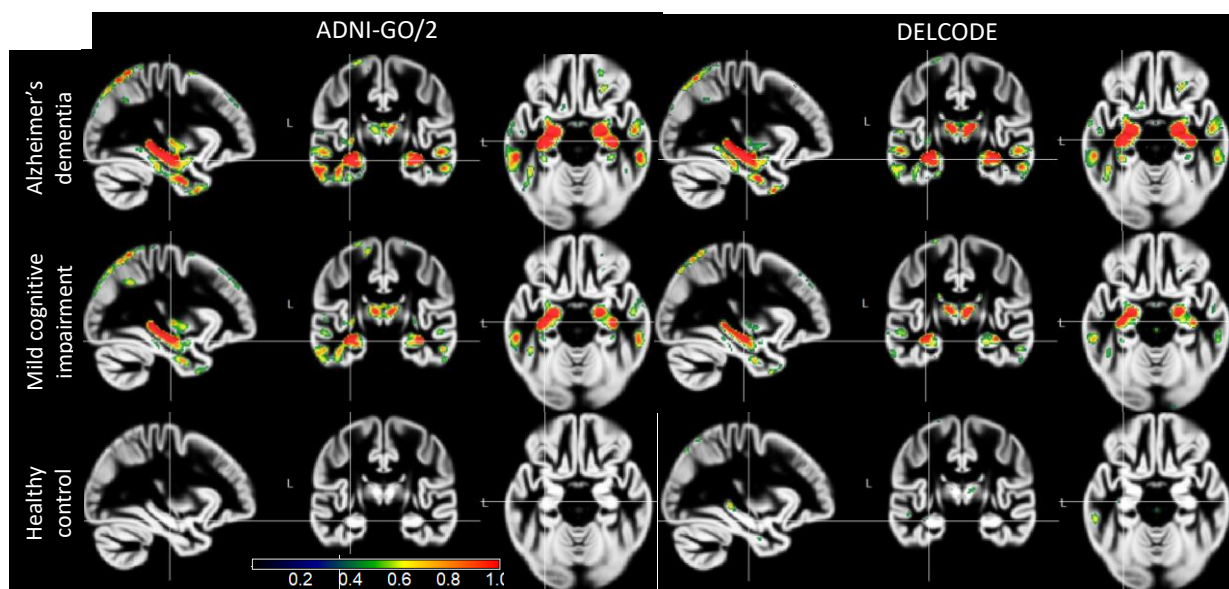
First block of CNN results reports values for accuracy etc. based on the optimal threshold identified from the training data. Second block of CNN results reports values based on the best threshold identified from post-hoc receiver operating characteristic analysis using the Youden index. Although this optimized threshold and derived performance values generally tend to overestimate the actual group discrimination ability of a model, they provide the upper bound of the accuracy that can be achieved by that particular model (see section 2.4 for details).

* Group separation based on hippocampus volume corrected for effects of the covariates age, sex, total intracranial volume and MRI scanner field strength using a linear model.

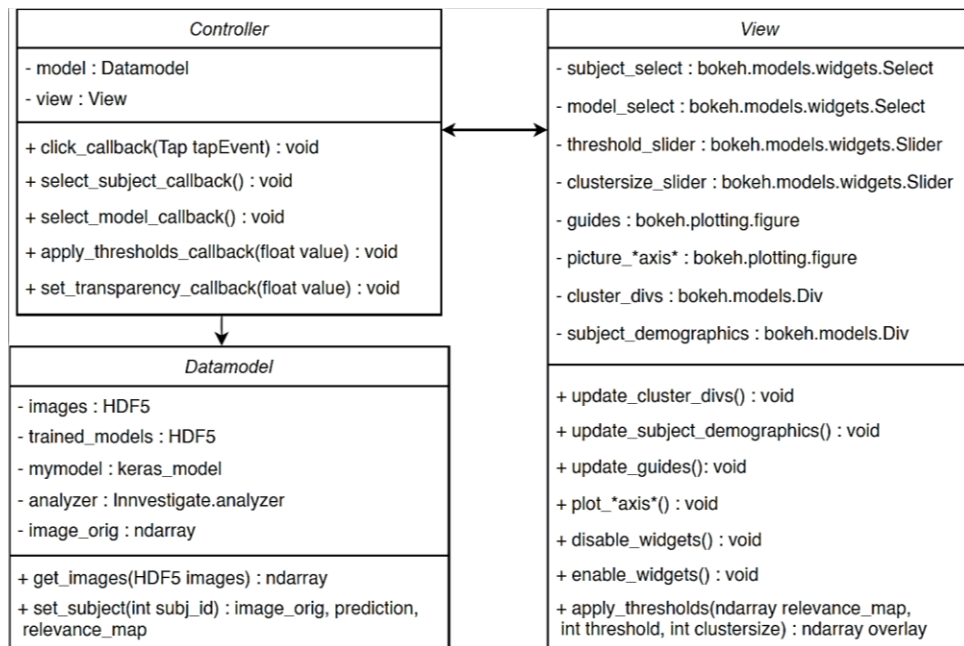
Supplementary Table 2 Group separation performance for hippocampus volume and the convolutional neural network models for raw input data.

Sample	Hippocampus volume*		3D convolutional neural network		
	Accuracy	AUC (CI)	Accuracy (SD)	Opt. accuracy (SD)	AUC (SD)
ADNI-GO/2					
MCI vs. CN	67.7 %	0.725 (0.680–0.771)	66.2 % (8.5)	72.6 % (9.5)	0.743 (0.120)
AD vs. CN	83.1 %	0.902 (0.871–0.928)	76.5 % (10.7)	85.1 % (6.8)	0.899 (0.089)
MCI ⁺ vs. CN ⁻	74.2 %	0.806 (0.754–0.852)	70.6 % (8.6)	77.3 % (9.9)	0.811 (0.128)
AD ⁺ vs. CN ⁻	84.6 %	0.912 (0.881–0.942)	78.3 % (11.6)	82.9 % (11.0)	0.903 (0.111)
ADNI-3					
MCI vs. CN	68.8 %	0.655 (0.604–0.703)	58.8 % (5.2)	65.9 % (2.9)	0.609 (0.017)
AD vs. CN	79.9 %	0.896 (0.841–0.945)	66.6 % (11.7)	85.6 % (3.3)	0.879 (0.024)
AIBL					
MCI vs. CN	82.4 %	0.737 (0.670–0.796)	58.9 % (9.3)	74.9 % (6.4)	0.710 (0.018)
AD vs. CN	88.8 %	0.895 (0.836–0.943)	60.8 % (11.7)	86.3 % (4.3)	0.904 (0.018)
MCI ⁺ vs. CN ⁻	87.3 %	0.737 (0.677–0.799)	61.4 % (10.5)	80.6 % (4.2)	0.795 (0.026)
AD ⁺ vs. CN ⁻	91.3 %	0.895 (0.837–0.943)	63.6 % (11.4)	87.5 % (3.5)	0.938 (0.018)
DELCODE					
MCI vs. CN	75.4 %	0.786 (0.736–0.831)	66.9 % (3.9)	71.3 % (2.0)	0.724 (0.028)
AD vs. CN	92.5 %	0.938 (0.903–0.968)	75.7 % (7.5)	86.9 % (2.9)	0.915 (0.015)
MCI ⁺ vs. CN ⁻	82.6 %	0.873 (0.798–0.934)	73.2 % (3.8)	75.8 % (2.0)	0.805 (0.024)
AD ⁺ vs. CN ⁻	93.5 %	0.950 (0.898–0.990)	81.4 % (6.4)	90.0 % (2.5)	0.944 (0.017)

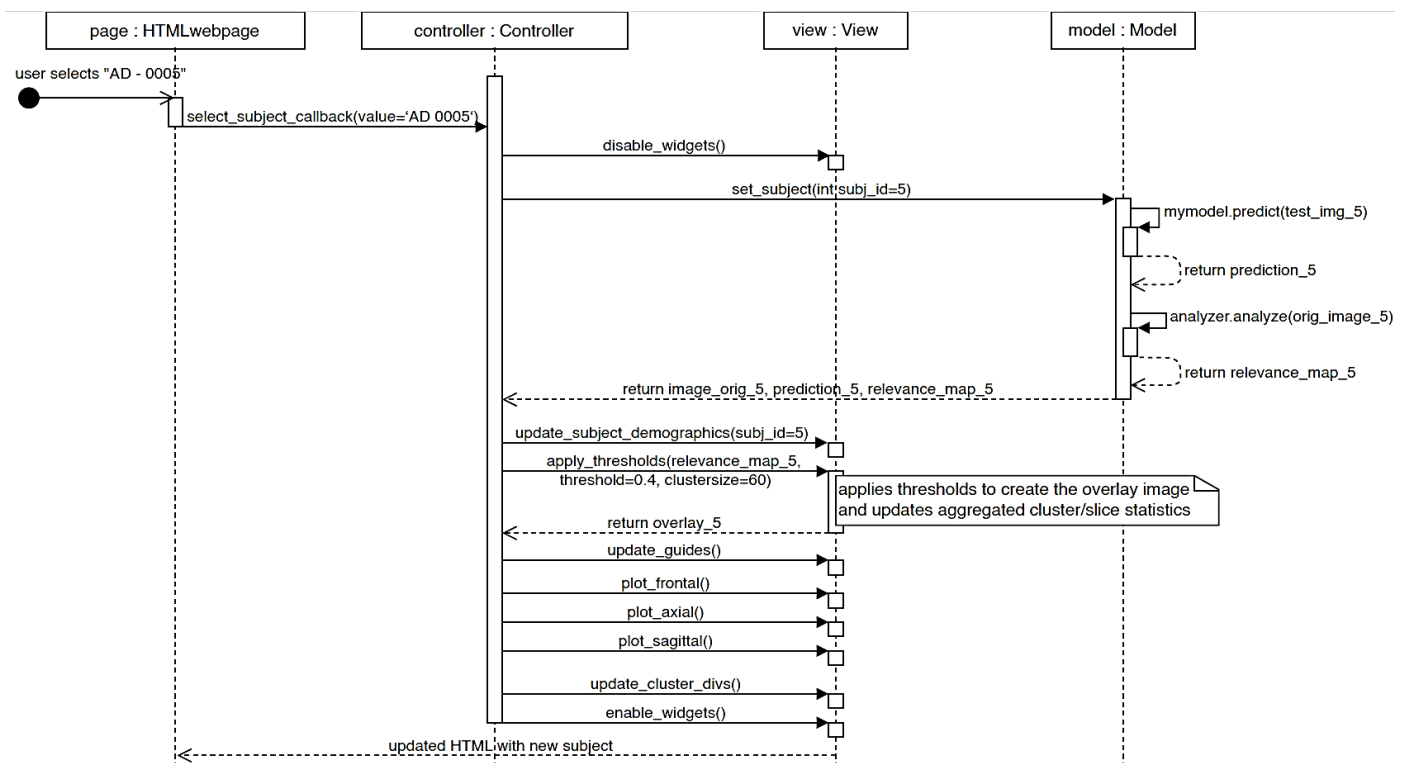
* Group separation based on hippocampus volume proportionally scaled to total intracranial volume.



Supplementary Figure 1 Comparison of mean relevance maps between samples. Left: ADNI-GO/2, Right: DELCODE.



Supplementary Figure 2 UML diagram of the interactive visualization application.



Supplementary Figure 3 Sequence diagram of function calls when selecting a new person.